Inertial Labs
a VIAVI Solutions company

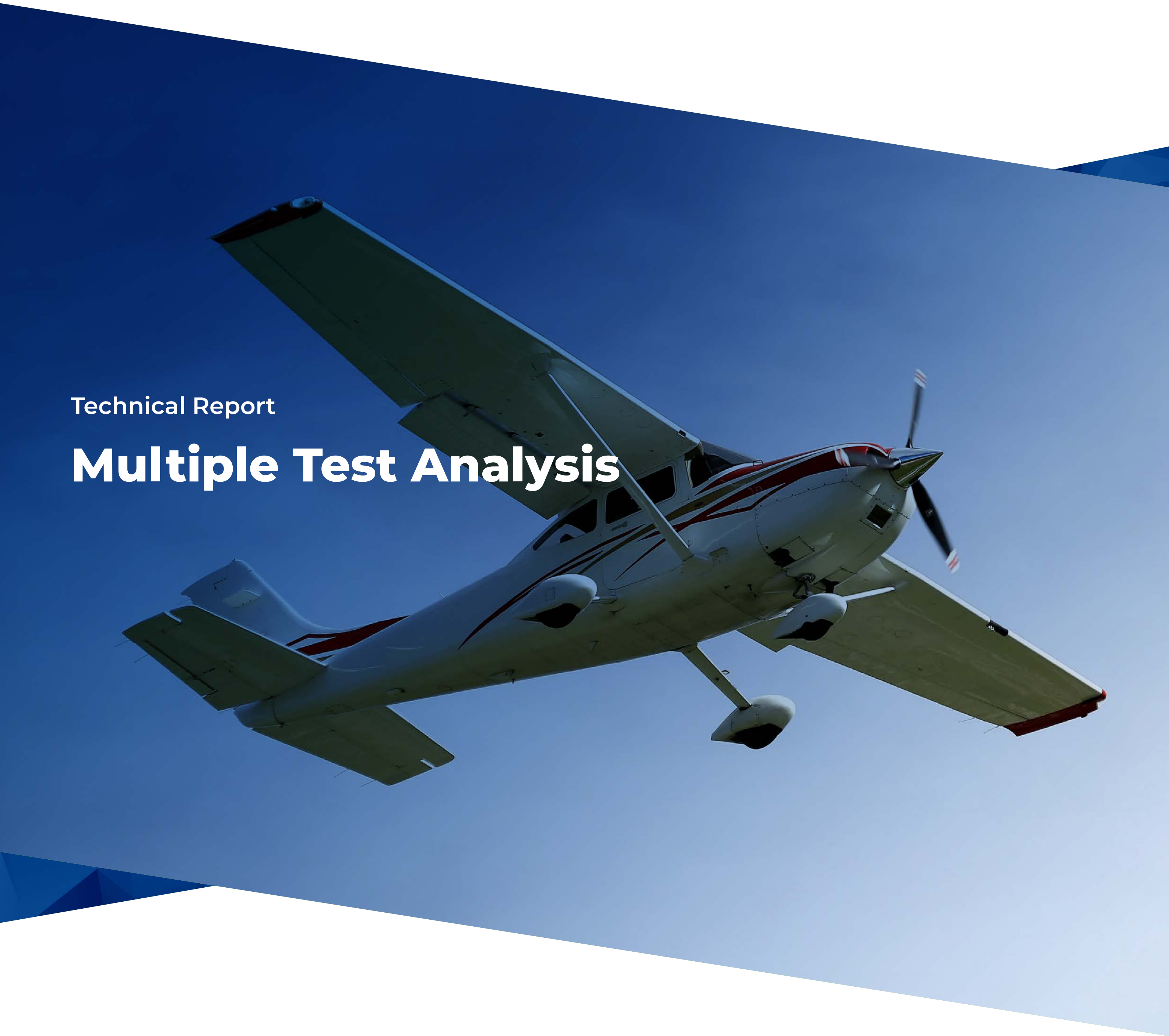

Technical Report

Multiple Test Analysis

October 2025

Table of Contents

1. Abstract

A set of flight tests onboard a Cessna 172 model S aircraft were conducted during daytime and evening conditions using both daylight and infrared cameras to evaluate the GNSS-denied performance of a VINS (Visual aided INS). The system utilized VIO (Visual Inertial Odometry) and VPS (Visual Positioning System) to aid navigation.

These systems maintain position accuracy during the GNSS-denied segment of the flight. During this phase, all GNSS updates were disabled, and the reported mean 3D position error of 16.55 meters was calculated exclusively from GNSS-denied data, with no contribution from GNSS aiding. This RMS value represents a single global error metric and is neither time nor distance dependent. The majority of each flight was conducted without GNSS.
The system maintained a CEP50 within a compact area over a 50 km trajectory at 13.22 meters, demonstrating stable and reliable positioning performance during GNSS-denied flight tests.

The flights were performed over visually challenging terrain, including mountainous regions, rivers, and agricultural zones, which are known to be difficult for vision-based systems. Table 1.1 summarizes the performance evaluation numbers that are analyzed from the flight tests with respect to ground truth references.

Table 1.1. Performance Table

Flight Date and Number	Position Error (m)	Maximum AGL (m)	Average AGL (m)	Flight Duration (min)	Flight Time in GNSS-Denied (min)	Distance Traveled (GNSS-Denied) (km)
2025-04-28-F1	14.32	1070.37	602.59	30.88	23.25	69.73
2025-04-28-F2	8.70	856.33	586.25	28.59	20.22	48.50
2025-04-28-F3	12.17	981.43	558.54	23.71	19.06	56.77
2025-06-05-F1	18.31	2078.25	1024.42	49.81	44.13	125.56
2025-06-05-F2	7.15	346.17	256.36	22.07	15.36	40.26
2025-06-21-F1	17.60	362.28	227.88	40.23	22.09	69.77
2025-06-21-F2	8.08	363.63	229.88	40.03	21.88	69.53
2025-06-21- F3	23.42	350.45	188.95	22.07	15.49	45.56
2025-06-21-F4	9.07	350.26	190.10	21.99	15.10	44.70
2025-06-25-F1	9.38	339.39	251.18	34.33	31.19	93.68
2025-07-10-F1	7.81	667.33	316.07	32.09	24.84	77.77
2025-07-10-F2	9.92	570.50	329.27	22.74	18.90	52.84
2025-07-10-F3	14.78	999.12	555.89	22.79	21.84	62.15
2025-07-10-F4	35.09	999.79	558.91	22.68	21.79	62.36
2025-07-22-F1	14.72	1285.08	922.00	36.81	28.32	101.15
2025-07-22-F2	11.38	1286.80	924.53	36.81	28.35	101.31
2025-07-22-F3	25.28	789.48	395.72	47.41	46.28	152.61
2025-07-24-F1	29.60	712.23	377.74	38.61	28.88	102.23

2. Introduction

This report presents an analysis of aerial GNSS-denied navigation performance using VINS, where visual map matching is fused with Inertial Labs' visual odometry to determine absolute position by comparing real-time imagery with onboard satellite-based 3D maps. Map matching will be referred to as the visual positioning system (VPS) and the Inertial Labs visual-inertial odometry as VIO.

The purpose of this study is to display the sensor fusion performance in GNSS-denied conditions of Inertial Labs VINS with VPS and VIO real-time visual map matching SDK. The SDK is able to provide absolute 3D positioning aiding data estimates to the INS's extended Kalman filter, resulting in highly accurate PNT information to end user applications.

The following paper will depict results from tests performed on a fixed wing, single engine vehicle. Table 2.1 shows the IMU and aiding data input sources that were used for the VINS platform during the test.

Table 2.1. INS Variant and Aiding data information

INS Variant	IMU Variant	Aiding Data Input
VINS	MiniAHRS (K100 IMU + Magnetometer)	VPS + VIO

2.1. Description of Aiding Data Input

VINS utilizes a robust visual map matching algorithm to estimate an aerial vehicle's absolute 3D position by applying computer vision principles to compare features captured from an onboard camera (day or IR (infrared) camera) with onboard satellite-based 3D maps for the VPS.

The position updates are computed at a data rate that varies based on the processor and are supplied as an aiding data source to the INS sensor fusion algorithm for correcting the INS position and velocity within GNSS-denied environments. In the case of an absence of VPS it relies on the VIO velocity estimation to estimate position.

3. Aerial Test Platform & Setup

Attached below are the figures that showcase how GNSS antennas and other subsystems were mounted onto the test aircraft for the VINS flight test. All flights were conducted using a Cessna-172 Skyhawk aircraft, which served as the primary aerial test vehicle.

Figure 3.1. Mounting of GNSS Antenna

Figure 3.2. Interface Connection Diagram & Setup of VINS

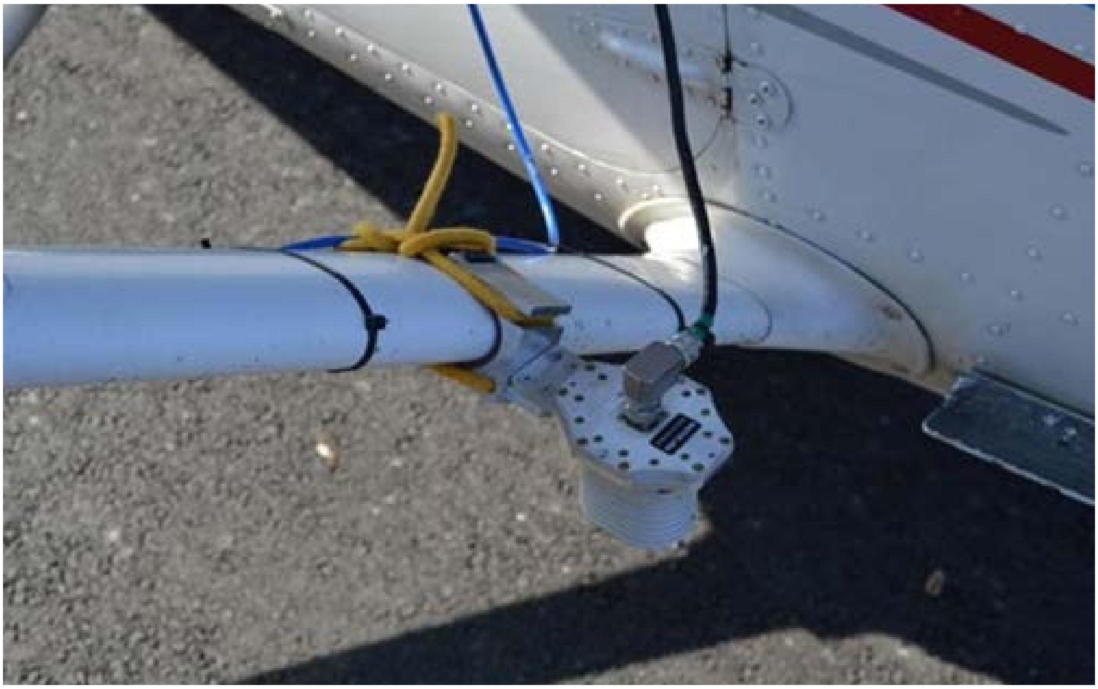

Figure 3.3. Mounting of Sensor Module on the Wing Strut

The sensor module was mounted on a wing strut, while the processing board was secured inside the aircraft cabin. Test flight was carried out at altitudes ranging from 200 to over 2000 meters above ground level to ensure sufficient distance from the ground for optimal ground speed performance while maintaining a safe margin from low-altitude hazards. Flying higher minimized noise in the camera data.

4. Flight Procedures

4.1. Initial Setup

Before takeoff, the aircraft remains stationary to allow the INS to complete a precise initial alignment. Using the web interface, the INS, GPS, and Camera systems were activated, and the initial altitude and current temperature were entered. These inputs were crucial for estimating atmospheric pressure and obtaining an accurate barometric altitude reading.

4.2. Magnetometer Calibration

After takeoff, a figure-eight maneuver is performed at around 400 meters AGL to calibrate the magnetometer. This ensures accuracy by compensating for environmental magnetic interference, which is critical for precise heading estimation. The maneuver was conducted at this altitude to comply with safety regulations and the proximity to Class B airspace.

4.3. GNSS-Denied Simulation

Following calibration, the aircraft climbed to the cruising altitude and aligned along pre-planned routes connecting local airports. Once stabilized on course, the GNSS system was disabled to create GNSS-denied environments. This allowed the sensor module to serve as the primary source for position estimation, enabling an evaluation of the system's performance without GNSS support.

5. Flight Procedures

19 different datasets were analyzed, with a focus on the GNSS-denied portions of the flight where the VINS operated without GNSS updates. In each case, the estimated position prior to integration into the INS was plotted alongside the resulting INS trajectory. The dark blue represents the true GNSS position, while the light blue represents the estimated position. The red squares present on the map depict the airports at which the flights were performed.

Across all datasets, the VINS trajectories remained closely aligned with the expected path. The system maintained performance across varying flight attitudes, altitudes, and during multiple turns, indicating that visual feature tracking remained reliable despite dynamic changes in motion. The second image illustrates the range of altitudes achieved, demonstrating the technology's capability to operate effectively both at low levels near the ground and at higher elevations, reaching up to 2 km AGL.

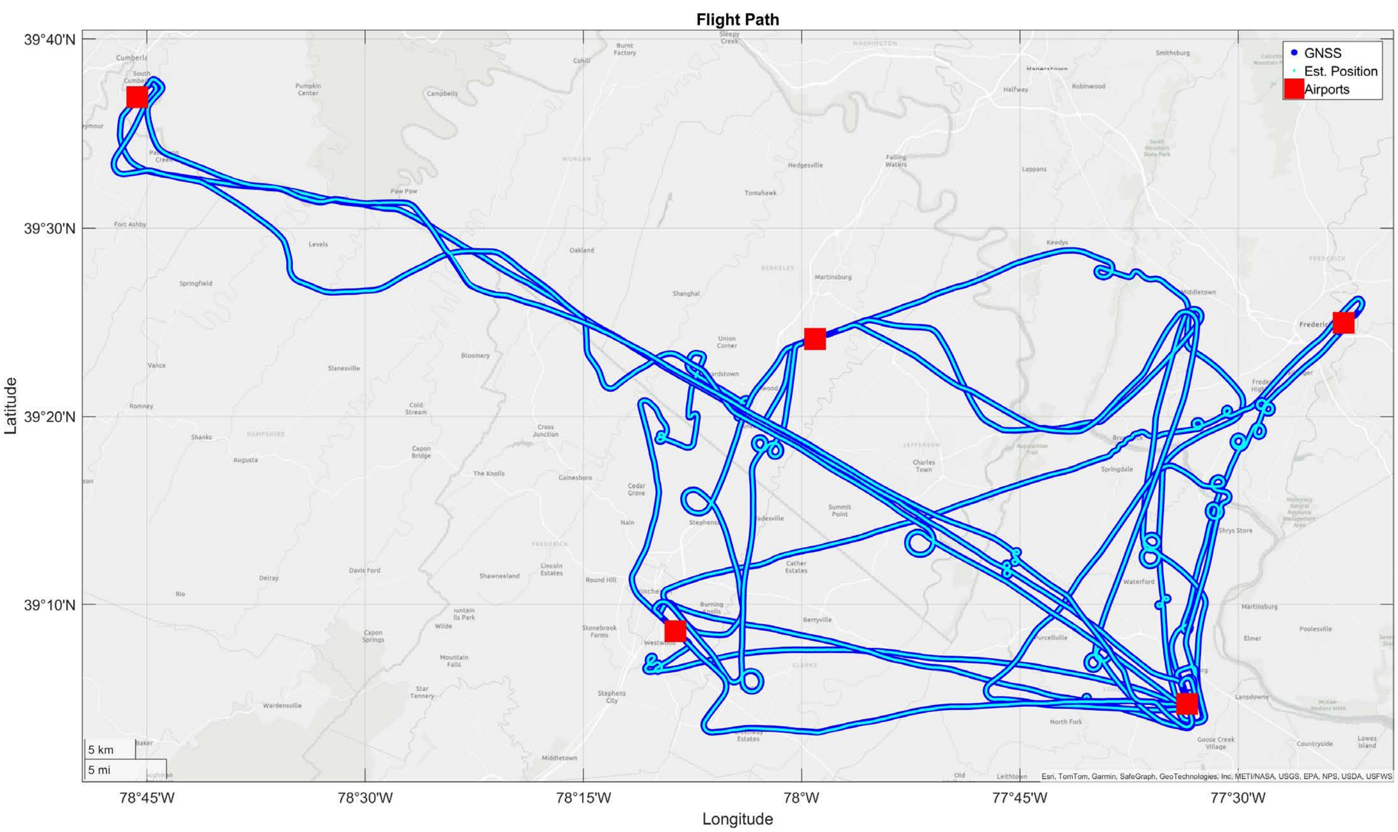

Figure 5.1. Flight Performance in GNSS denied environment

The majority of the flights were conducted at low altitude to create a more challenging operating environment and to replicate scenarios closely aligned with the anticipated use cases of our customers.

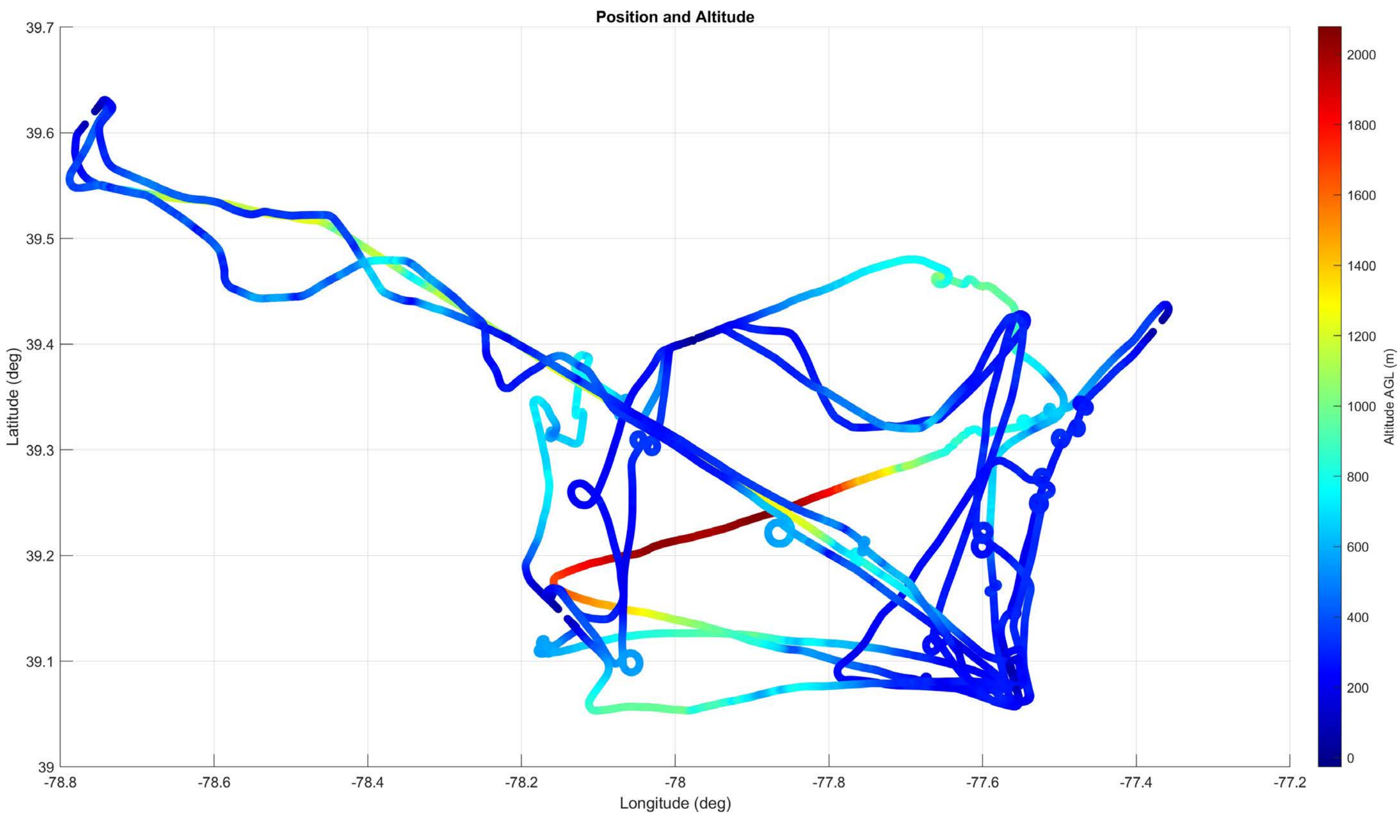

Figure 5.2. Longitude, Latitude and Altitude Comparison

Figure. 5.3 presents the Northing and Easting position errors across the 18 GNSS-denied flight datasets, plotted as a function of time. Each trajectory corresponds to a distinct test flight, as indicated in the legend. These plots provide a quantitative view of how lateral position errors evolved during extended periods of GNSS outage. In the Northing error subplot, most trajectories remain within ±50 meters of the reference path for the majority of the flight.

A few datasets; particularly 2025-07-24-F1 and 2025-07-22-F3, show larger deviations beyond 80 meters, primarily during the final segments of the flight. This degradation does not correlate with increased flight duration, rather the area flown over to challenge the VPS system.
The Easting error subplot reveals a similar trend: errors are typically bounded within ±50 meters.

The error spikes are likely linked to scenarios in which aiding sources (e.g., map matching or visual odometry) became less effective due to degraded visual conditions or poor visual references. Despite the increased error in some cases, the majority of datasets remain without any free inertial drift, indicating that the integration of map matching and visual odometry provided consistent correction throughout most of the trajectory. The bounded nature of the drift in all datasets, with few exceeding 100 meters, further supports the system's robustness in GNSS-denied environments, even under varying altitudes and motion dynamics.

Figure 5.3. Easting and Northing Error

Figure. 5.4 presents the probability distribution of the mean error position between Easting, Northing and Up positi on point by point on each flight. This plot illustrates the overall likelihood for different positional errors within each dataset, providing a statistical perspective on the navigation system's accuracy when relying on VPS+VIO.

Each curve represents the distribution of error values observed during the flight, with higher peaks indicating that the error remained consistently bounded around a specific range, while flatter, more spread-out curves suggest greater variability and less constrained drift. Most datasets exhibit a prominent concentration of error below 40 meters, highlighting that in typical scenarios, the position estimates remain tightly clustered and controlled.

This region of overlap across multiple flights defines a performance envelope that can be used as a benchmark for expected system behavior. For example, the narrow, high peaks of datasets like 2025-06-05-F1 and 2025-06-21-F4 reflect stable performance with minimal drift, while the broader curves seen in datasets such as 2025-07-24-F1 reveal cases where the system experienced more challenging conditions.

This probabilistic view offers a valuable summary of expected positioning performance using VINS, in GNSS-denied environments. It not only helps identify outlier conditions but also establishes a common bounded error region within which future tests and customer deployments are likely to operate. By observing where most datasets align, the plot provides practical guidance for performance expectations and acceptance criteria in real-world applications.

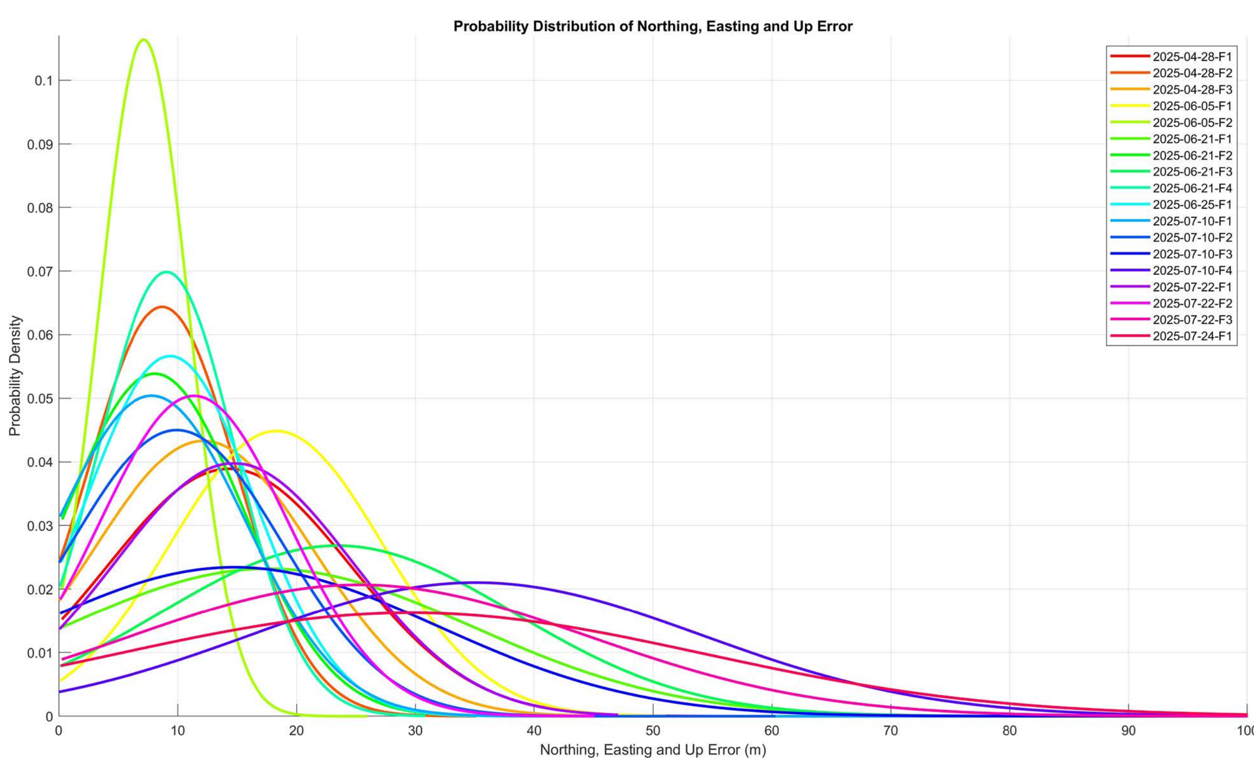

Figure 5.4. 3D Position Error Probability plot

Figure. 5.5 presents the global probability distribution of the Easting, Northing and Up position across all eighteen test flights. The function demonstrates the probability of errors across all combined flights. Shown is the mean error, which sits at 16.55 meters.

The distribution is positively skewed, meaning that smaller errors occur more frequently, while larger errors, extending to nearly 100 meters, are rare and have very low probability. This reflects that the VPS and VIO system lead to generally high positional accuracy, with deviations being far less frequent.

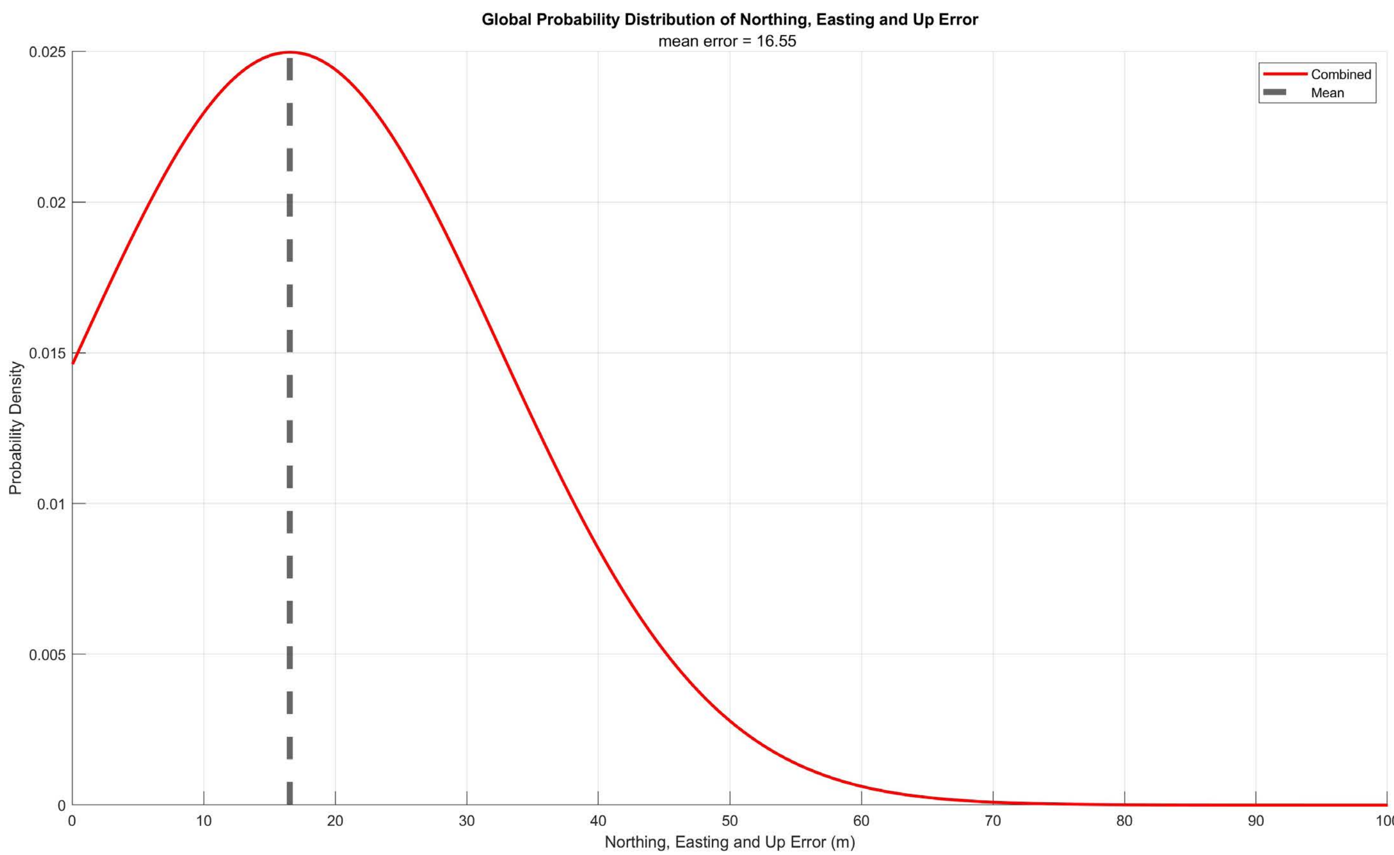

Figure 5.5. Global Probability for Northing, Easting, and Up Error

Figure. 5.6 shows the position error relative to the total distance traveled for each GNSS-denied flight in percentage, offering insight into the system's scalability and consistency over long trajectories. Since the navigation system fuses VPS data with VIO, this plot helps characterize how effectively the system maintains positional accuracy across increasing distances. The error remains well-contained (typically below 0.2% DT) for the majority of each dataset, indicating consistent performance in normal conditions.

A hyperbolic decay pattern emerges clearly, as expected, reflecting how the error per distance traveled decreases when the system is regularly corrected by VPS updates. VPS aligns the estimated position with known features, thereby bounding drift around a reliable reference. Spikes in the plot, such as those seen in 2025-07-24-F1 and 2025-07-10-F3, correspond to intervals where VPS matching deteriorates and VIO takes over.

These dynamics underscore the layered reliability of the navigation architecture: when VPS confidence drops, VIO ensures continuity, and when both are compromised, the system degrades to inertial dead reckoning. Despite these transitions, the system demonstrated high robustness even over a 100 km flight, the total accumulated error remained slightly lower than 0.2% (500 meters) before starting the approach to land.

This validates the system's capability to combine multiple aiding technologies while maintaining precise and resilient navigation in GNSS-denied environments.

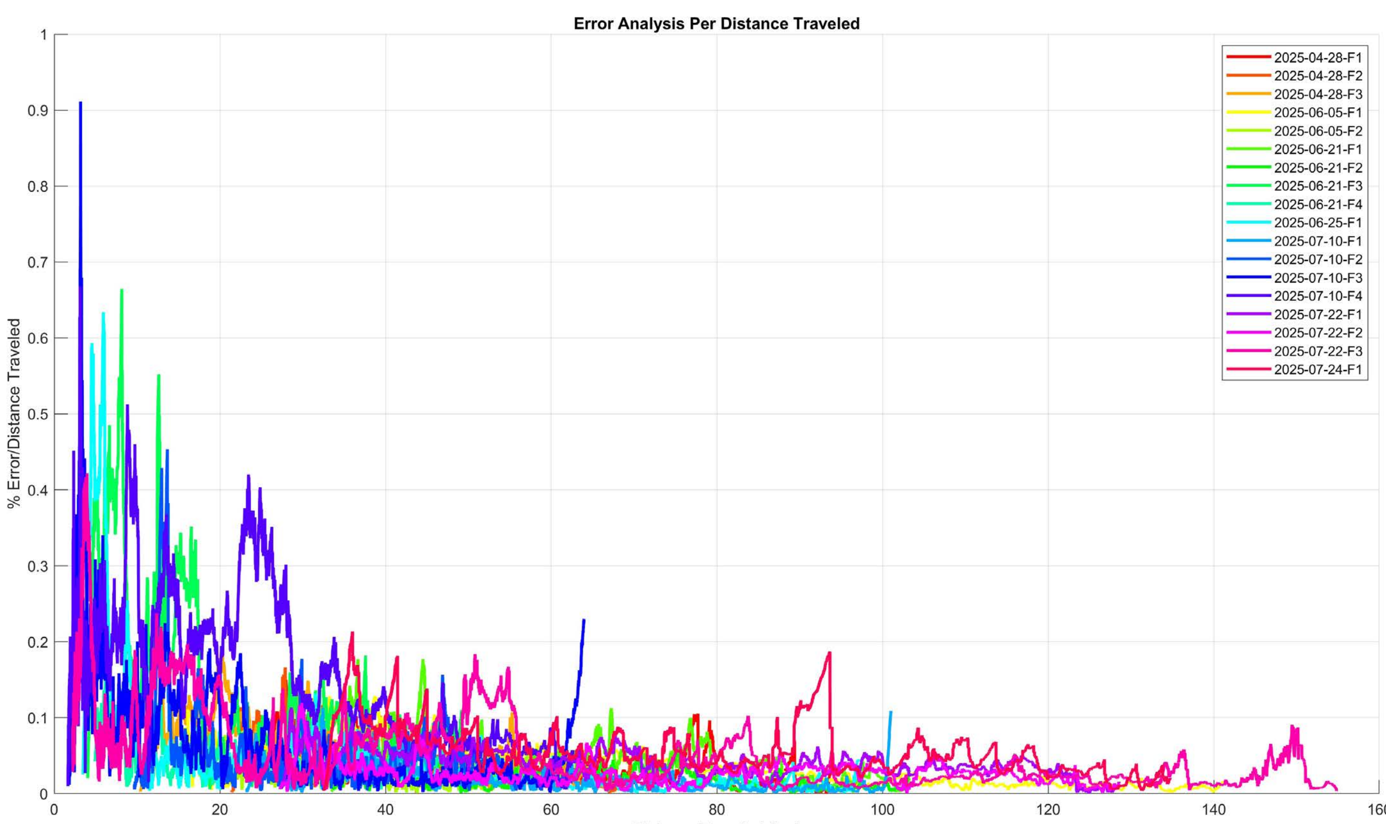

Figure 5.6. Error Analysis per Distance Traveled

Figure. 5.7 presents the probability distribution of the normalized position error growth rate, expressed as percentage per unit distance traveled, across all datasets. The majority of datasets were concentrated at lower %/distance values, indicating the capacity of VINS with VPS and VIO to maintain high positional stability, with error increasing only minimally over the course of travel.

Broader or right-shifted distributions such as 2025-06-21-F3 suggest conditions where error accumulated more rapidly, reflecting greater drift per unit distance. The concentration of probability mass near low values establishes a benchmark region of expected stability, while the tails of the distribution reveal fewer common scenarios where performance was challenged.

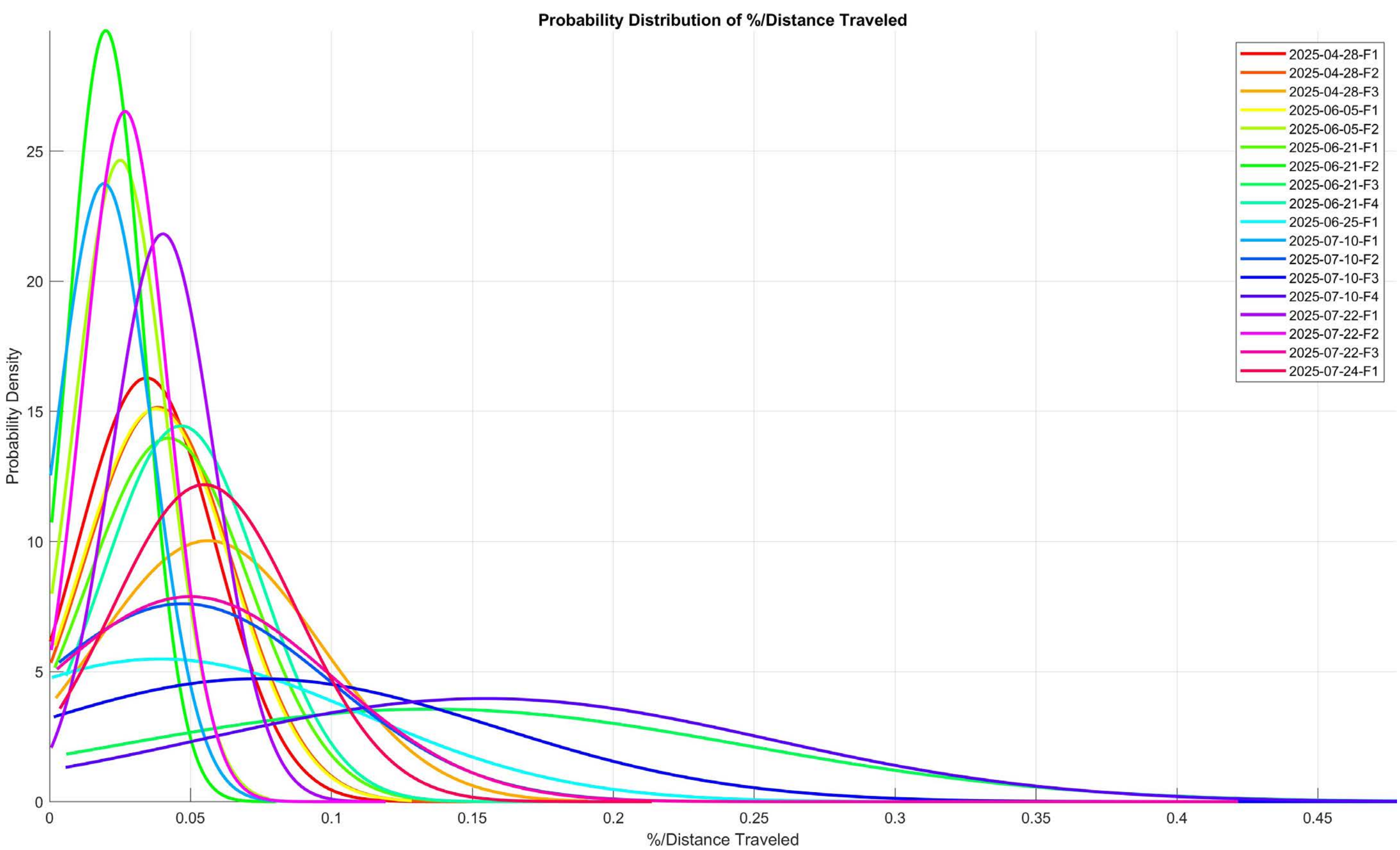

Figure 5.7. Probability Density vs %/Distance Traveled

Figure. 5.8 presents the Circular Error Probable (CEP) plot. It illustrates the horizontal positional accuracy of the VINS system by showing the area within which 50% of the GNSS-denied position estimates fall over a 50 km trajectory. The calculated CEP50 for these datasets was 13.22 meters. The center of the circle represents the true position, while the plotted data points represent the system's estimated positions. A smaller CEP indicates tighter clustering of position estimates, meaning higher consistency and reliability of the navigation solution. In this case, the CEP demonstrates that even during extended GNSS-denied flights, the majority of position errors remain within a constrained region, highlighting the system's ability to maintain stable tracking over long distances.

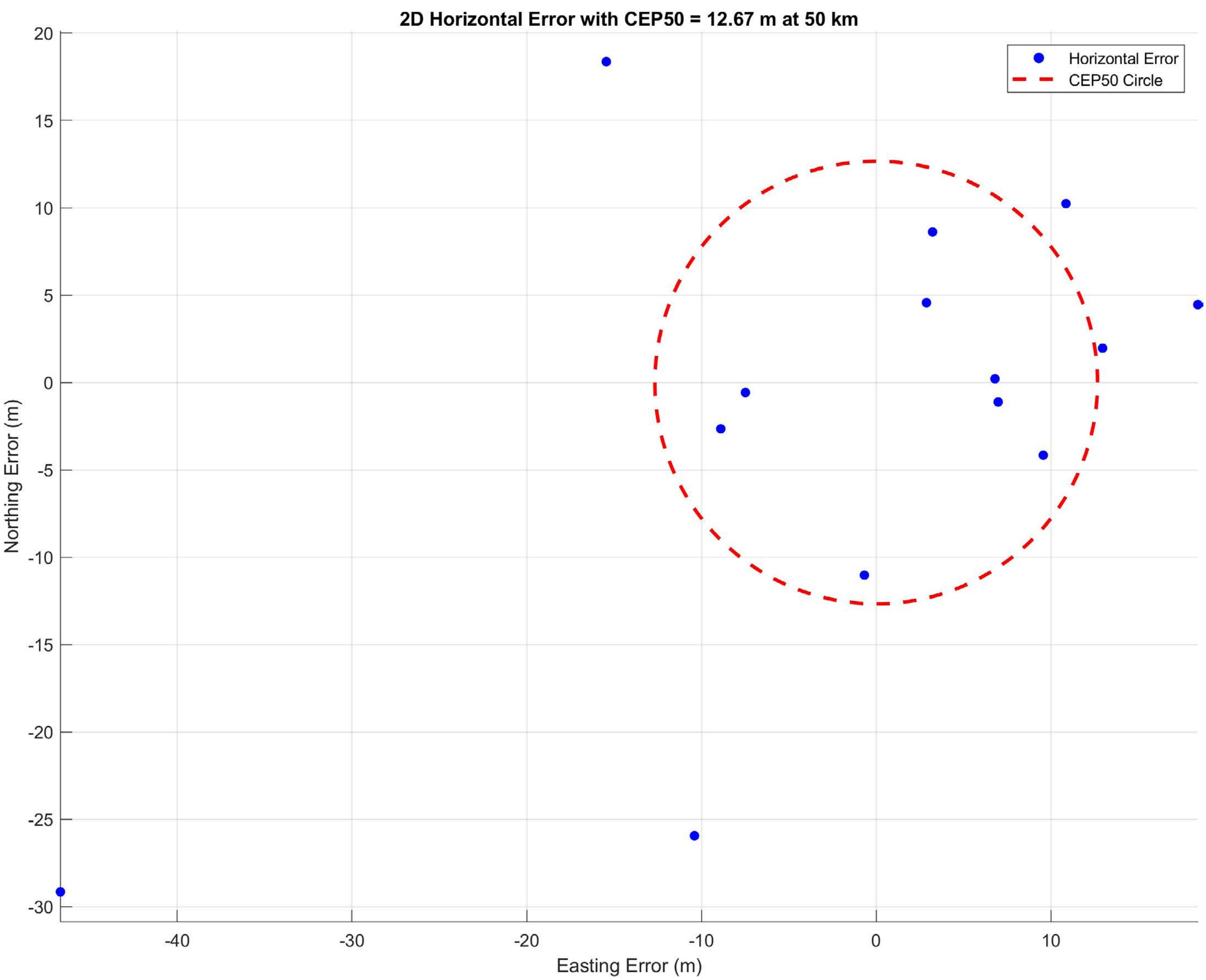

Figure 5.8. Circular Area Probable 50% at 50km

6. Boson Infrared Camera

This chapter presents an evaluation of the BOSON infrared camera. Given the IR camera's critical role in night operations, all BOSON-based test flights were conducted in the evening hours. This methodology was selected to assess system robustness across varying environmental conditions and times of day. The inclusion of IR capability enhances operational flexibility by enabling consistent performance in both daylight and nighttime scenarios, while also mitigating the effects of cloud cover on visual sensing.

As shown in Figure. 6.1, the set of flights to be analyzed in this section were performed at the Leesburg, Frederick, Martinsburg, and Winchester regional airports .

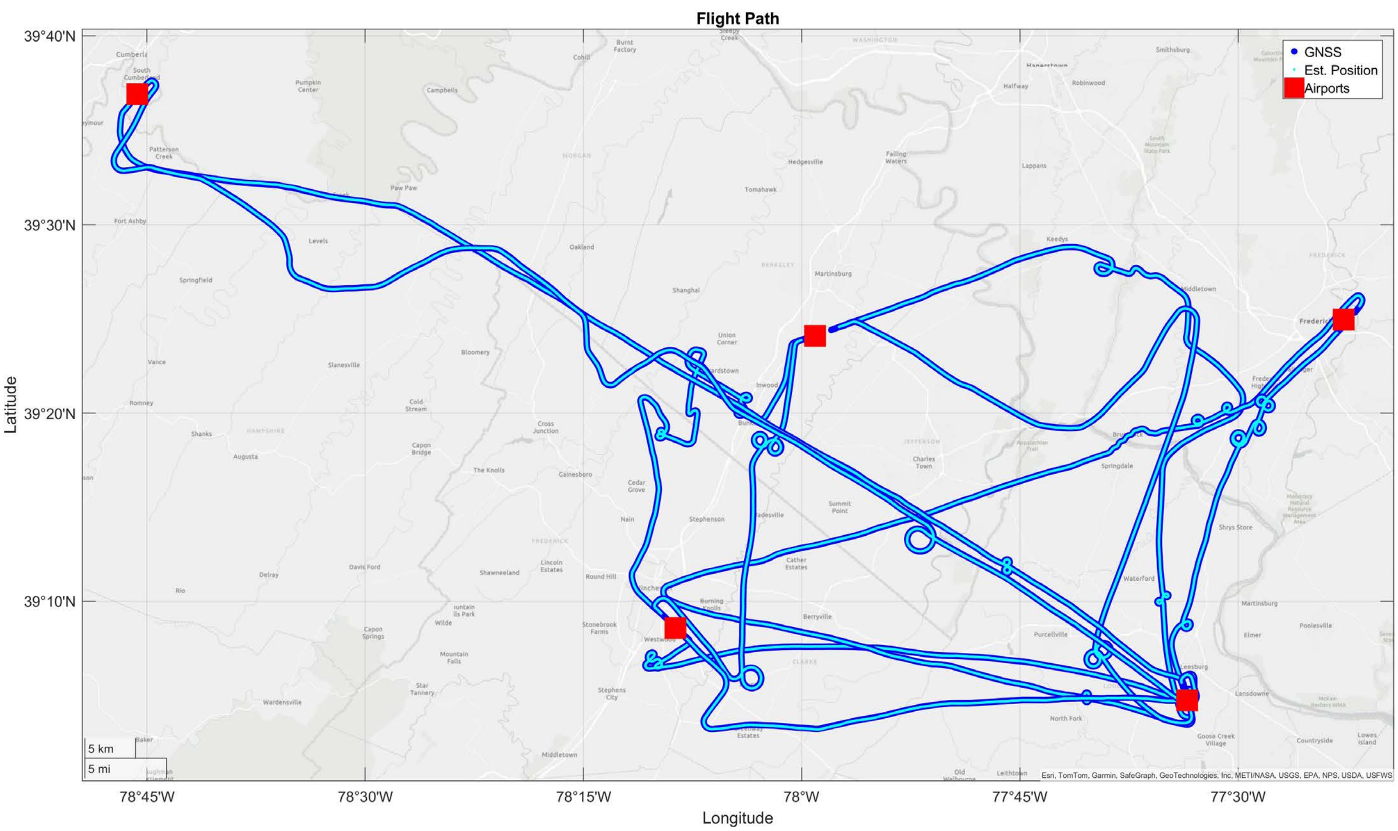

Figure 6.1. Flight Performance in GNSS denied environment

The flights were primarily flown at low altitudes to ensure a higher challenge to the VPS. The highest attained altitude was 2000m AGL, with flights typically ranging from 225 to 550m AGL. Lower flights could not be performed due to safety restrictions.

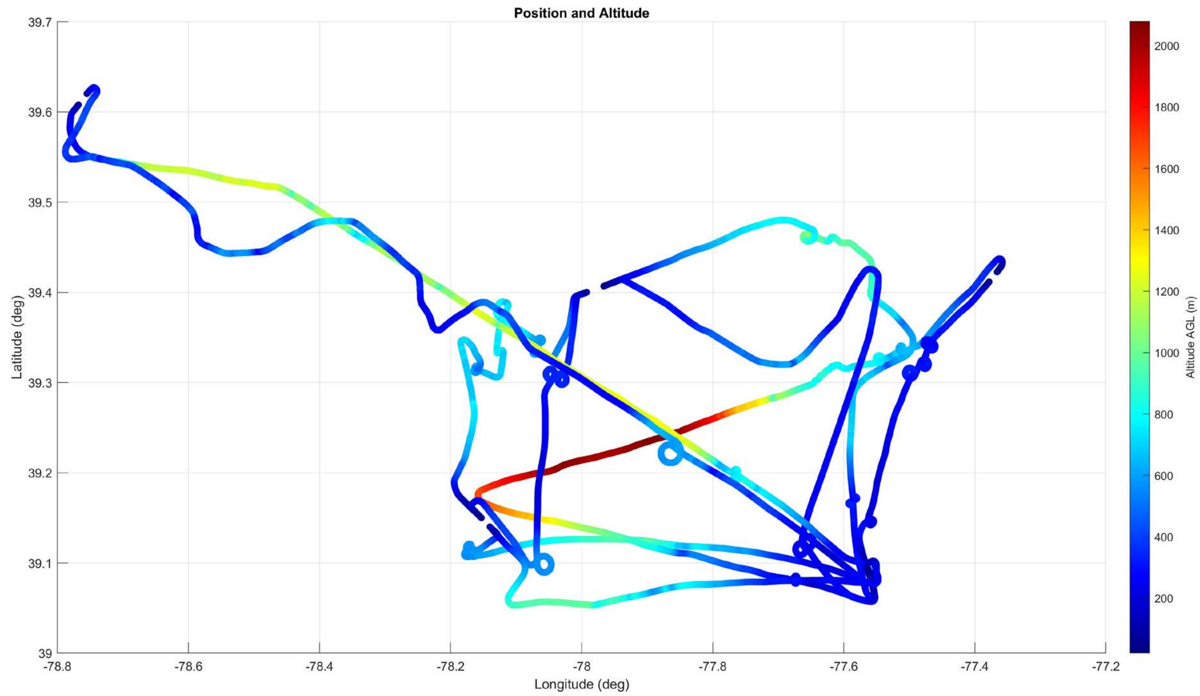

Figure 6.2. Longitude, Latitude and Altitude Comparison

Figure. 6.3 presents the Northing and Easting position errors across the GNSS-denied flight datasets, plotted as a function of time. These plots provide a quantitative view of how lateral position errors evolved during extended periods of GNSS outage. In the Northing error subplot, the trajectories remain almost entirely within ±50 meters of the reference path for the majority of the flight.

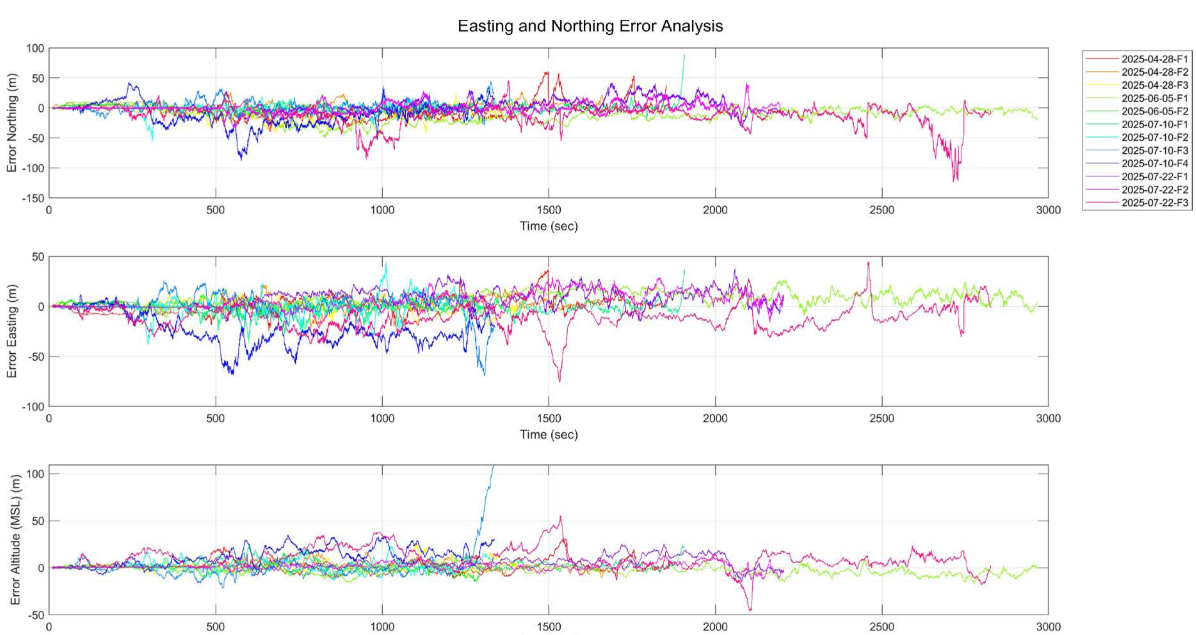

Figure 6.3. Easting and Northing Error

One dataset, 2025-07-10-F4, increased beyond the ±50 meters mark, however it only increased by around 10 meters. The Easting error subplot reveals a similar trend: errors are generally bounded within ±50. Flights like 2025-07-22-F3 experience a rise in error towards the end of the flight due to the terrain and altitude as approaching landing. The bounded nature of the drift in all datasets, with few exceeding 50 meters, further supports the system's robustness in GNSS-denied environments, even under varying altitudes and motion dynamics.

Figure. 6.4 presents the probability of distribution of the mean error position between Easting, Northing and Up position point by point on each flight. Most datasets exhibit a prominent concentration of errors below 20 meters, showing that the position estimates are often highly accurate. The wider curves seen in datasets such as 2025-07-10-F4 reveal cases where the system experienced more challenging conditions , such as the mountainous terrain being flown over.

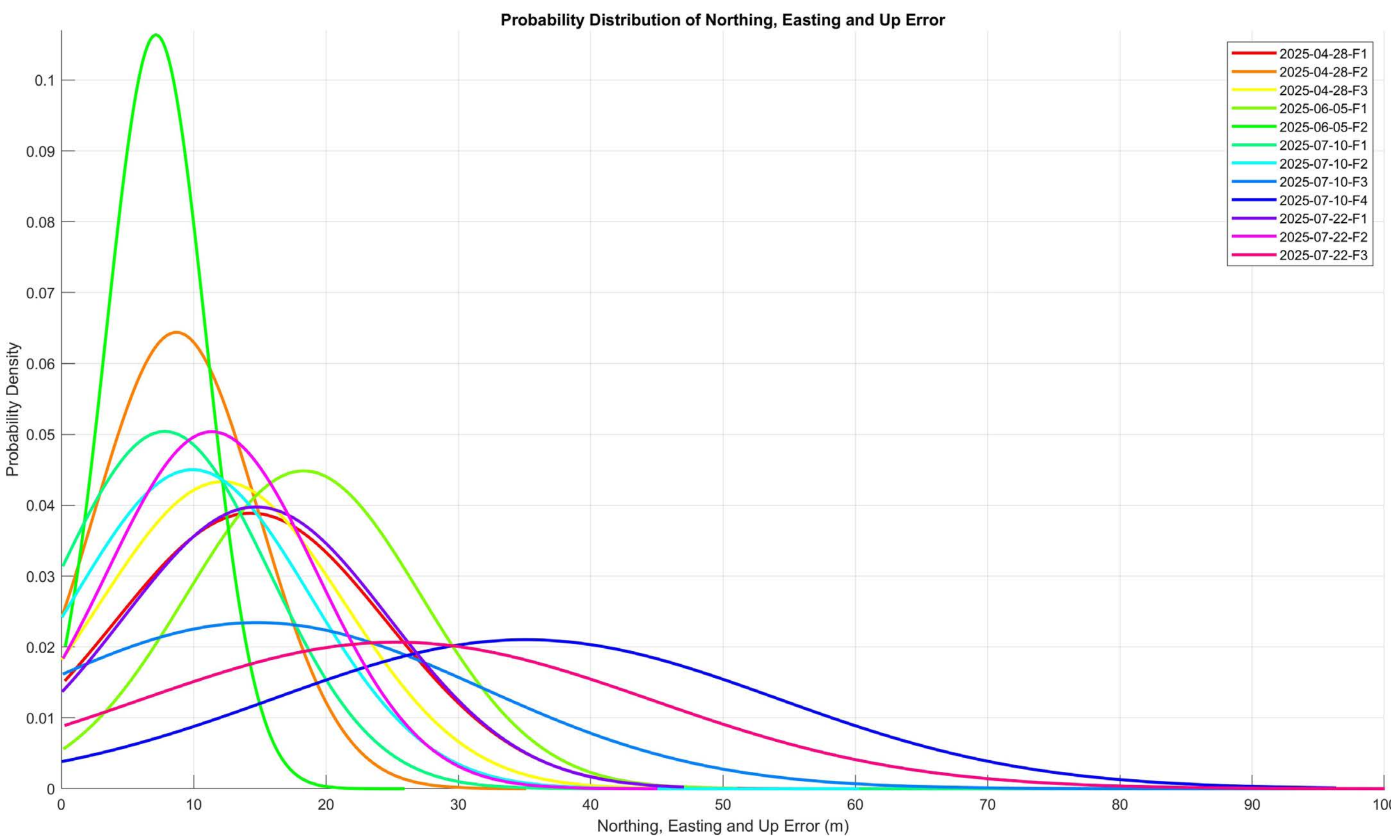

Figure 6.4. 3D Position Error Probability plot

Figure. 6.5 shows the global probability distribution of the combined Northing, Easting, and Up positional errors, measured in meters, across all 12 datasets. The calculated mean error is 15.88 meters, showing the capability of the system to perform with low drift while flying at low altitudes. The distribution is positively skewed, meaning that smaller errors occur more frequently, and that errors beyond 65 meters are improbable.

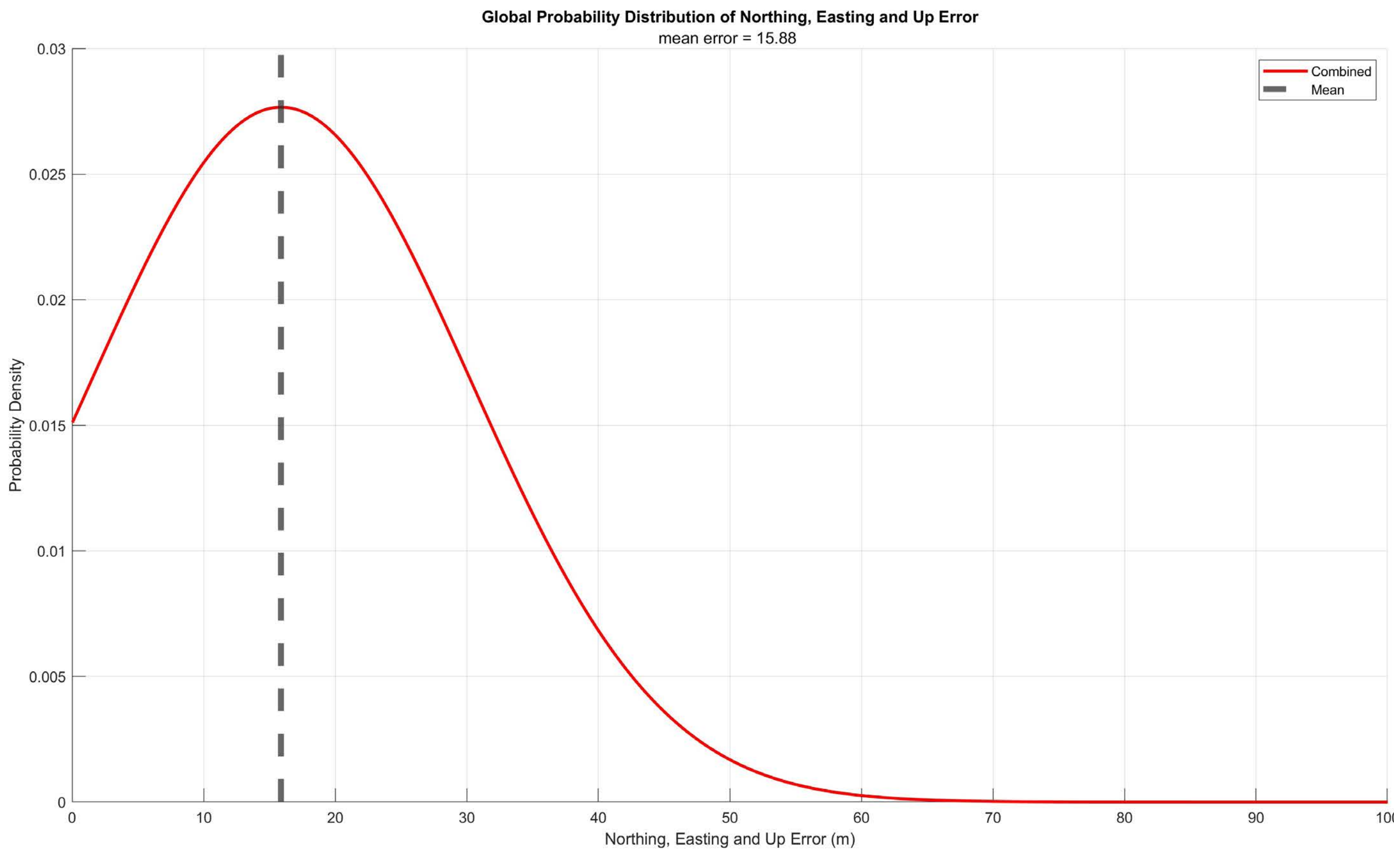

Figure 6.5. Global Probability for Northing, Easting, and Up Error

Figure. 6.6 presents the error growth rate per unit traveled, expressed as percentage per kilometer, for multiple flight datasets. Across all datasets, the error rate is generally highest in the initial phase of travel, in which the system is initialized. As the distance increases, most datasets show a rapid reduction in error growth rate, typically falling below 0.1%/km after approximately 20 km.

Certain datasets, such as 2025-07-10-F4, exhibit greater variability and higher peaks early in the trajectory, indicating more challenging conditions during the initial segment. In contrast, flights like 2025-04-28-F1 maintain consistently low error rates once stabilized.

Overall, the convergence of error growth rates to low, stable values over extended distances highlights the system's ability to effectively constrain drift when using VPS+VIO in GNSS-denied environments, even after periods of higher initial uncertainty.

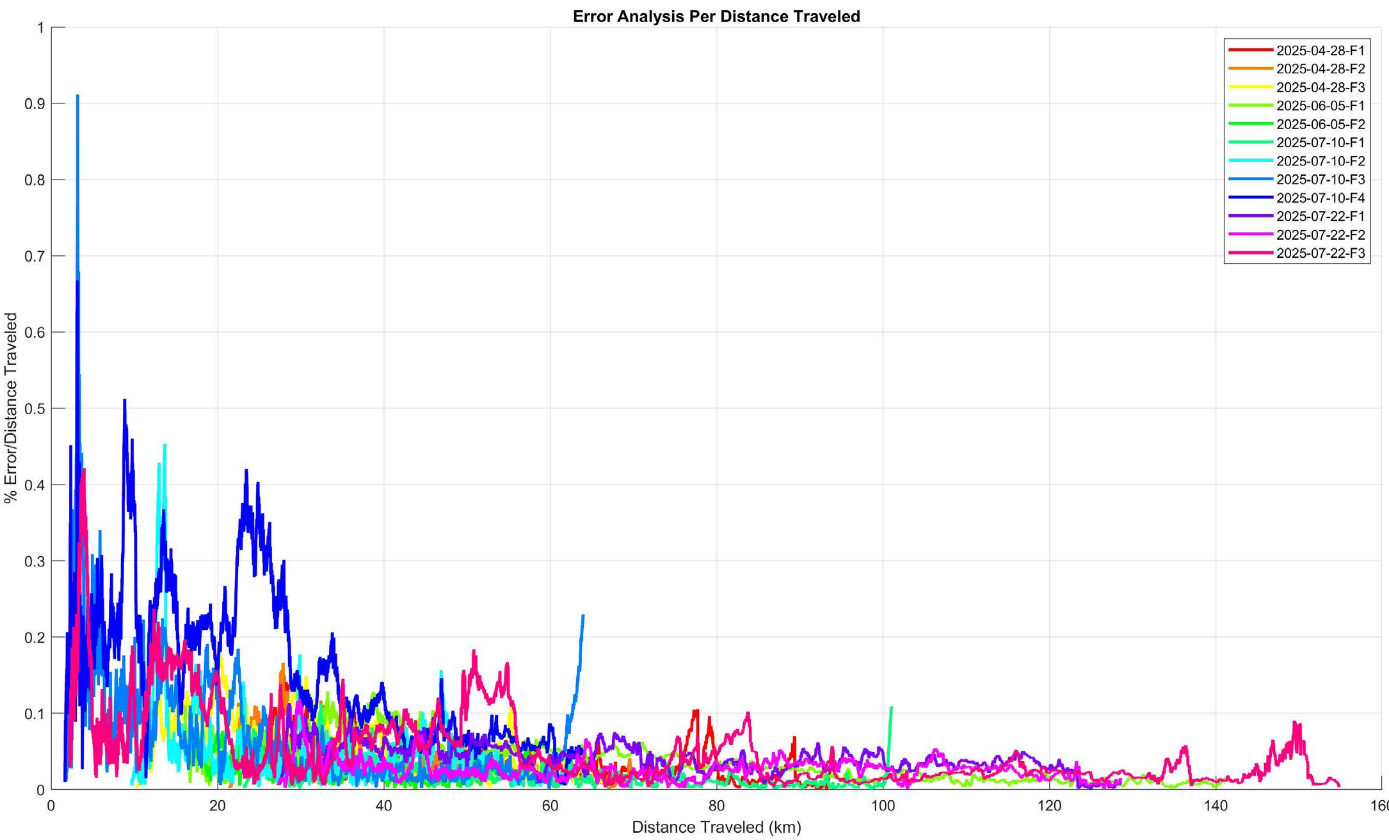

Figure 6.6. Error Analysis per Distance Traveled

Figure. 6.7 presents the probability distribution of the normalized position error growth rate, expressed as percentage per unit distance traveled, across all datasets. The majority of datasets were concentrated at lower %/distance values, indicating the capacity of VINS with VPS and VIO to maintain high positional stability, with error increasing only minimally over the course of travel.

Broader or right-shifted distributions such as 2025-07-10-F4 suggest conditions where error accumulated more rapidly, reflecting greater drift per unit distance.

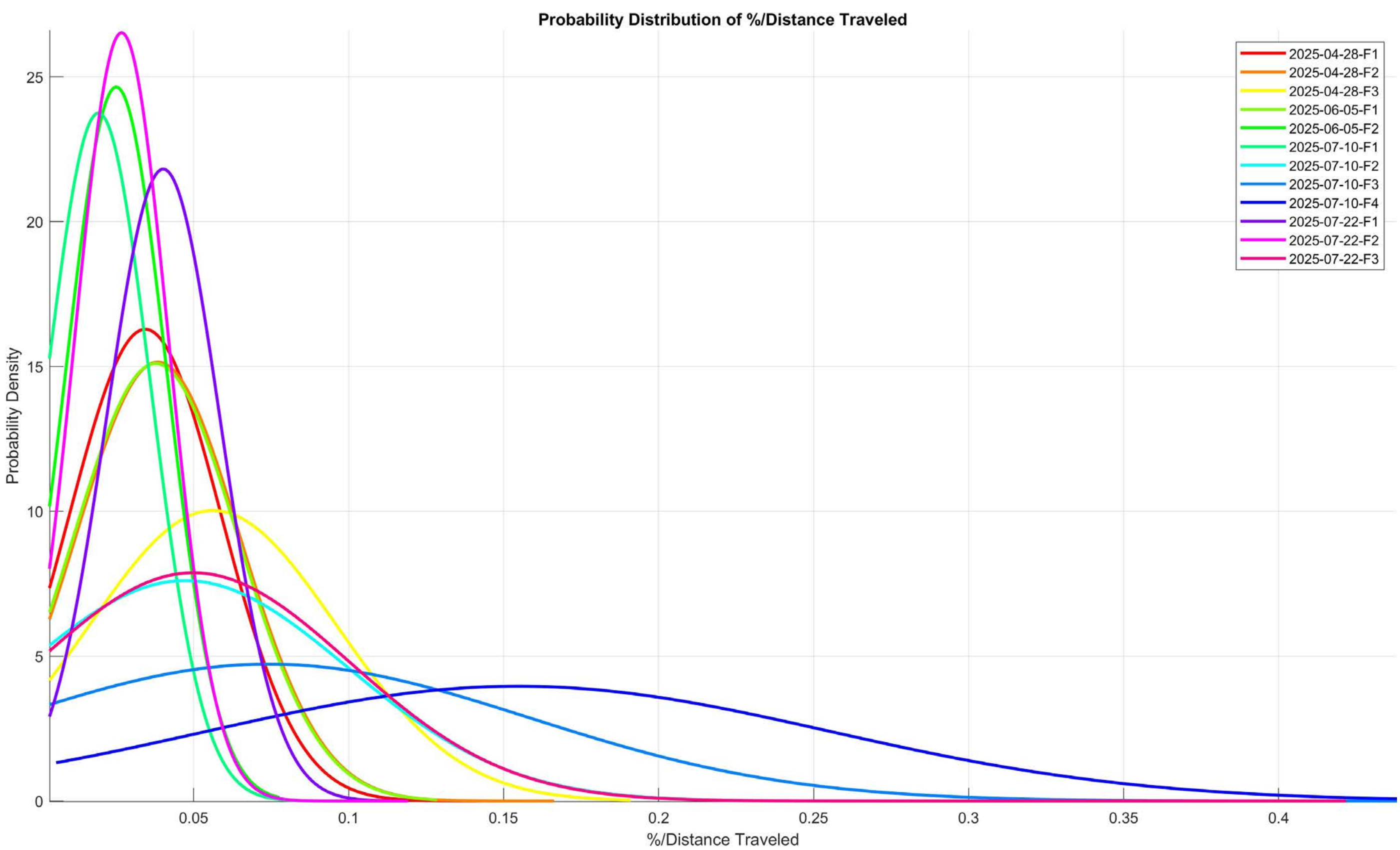

Figure 6.7. Easting, Northing and MSL error vs DT in percentage

7. Blackfly Daycam

This chapter presents an evaluation of the Blackfly Daylight Camera. This methodology was selected to assess system robustness across typical daytime operations. Flights were performed during daylight hours, across multiple terrain types and weather conditions.

As shown in Figure. 7.1, the flight analyzed was performed between the Leesburg, Martinsburg, Winchester and Cumberland regional airports. The routes were chosen as they are not densely populated, allowing the VINS system to be tested over remote regions with fewer distinguishing landmarks.

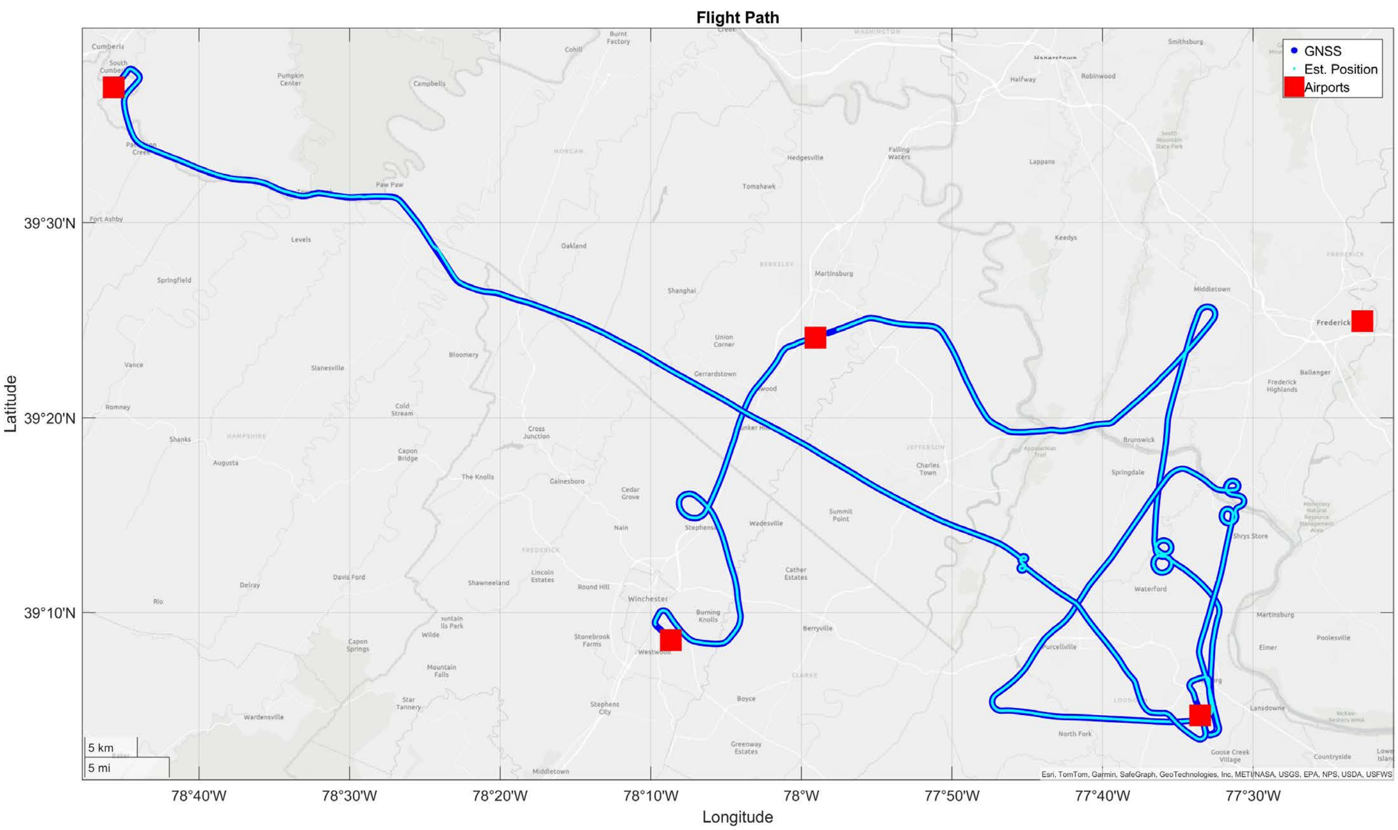

Figure 7.1. Flight Performance in GNSS denied environment

The flights were conducted at altitudes ranging from 250 m to 700 m, with the majority of operation occurring between 250 m and 350 m. Variations in altitude, including climbs and descents, were driven by the mountainous terrain over which the flights took place.

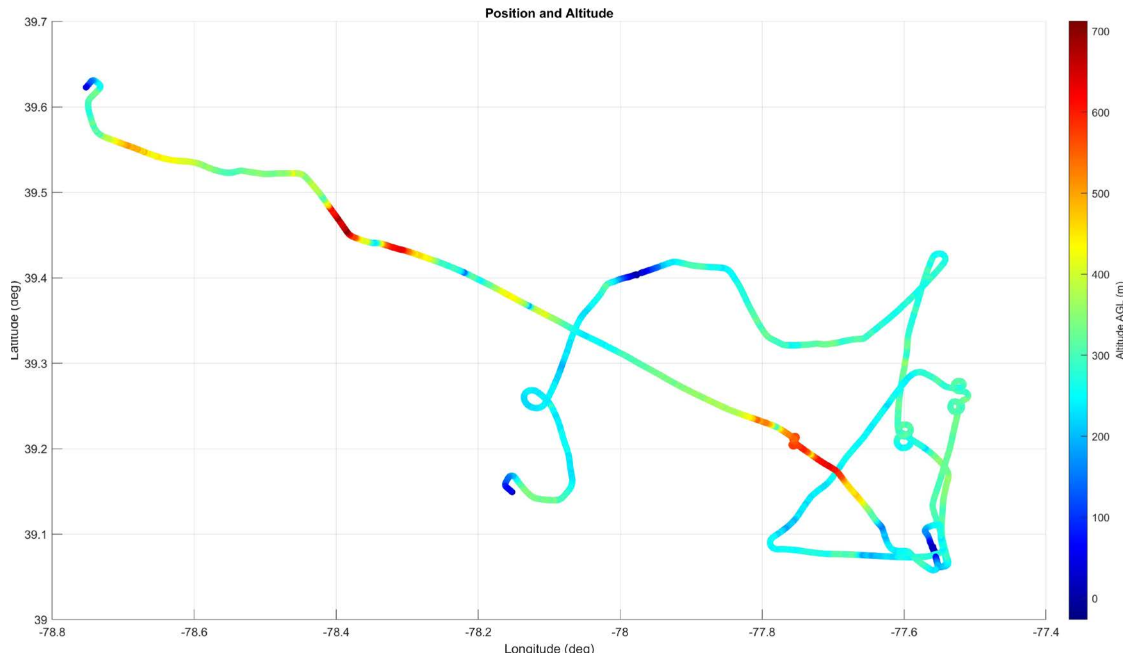

Figure 7.2. Longitude, Latitude and Altitude Comparison

Figure. 7.3 presents the Northing and Easting error, shown as a function of time. In the Northing error subplot, most of the flights were bounded between ±50 meters, with a spike to around 150 meters before returning to the ±50 mark.

The Easting subplot performed even better, with an error bounded nearly entirely within ±50 meters. There was a spike to around -75 meters, but similarly to the Northing plot, it shortly returned to average. The ability to course correct shows the capability of the VINS system over challenging terrain areas.

Figure 7.3. Easting and Northing Error

Figure. 7.4 presents the probability distribution of the mean error position between Easting, Northing and Up position point by point. Most datasets showed a concentration of errors at or below 20 meters, demonstrating highly accurate position updates. The wider curves seen in datasets such as 2025-07-24-F1 show cases where the system experiences more challenging conditions.

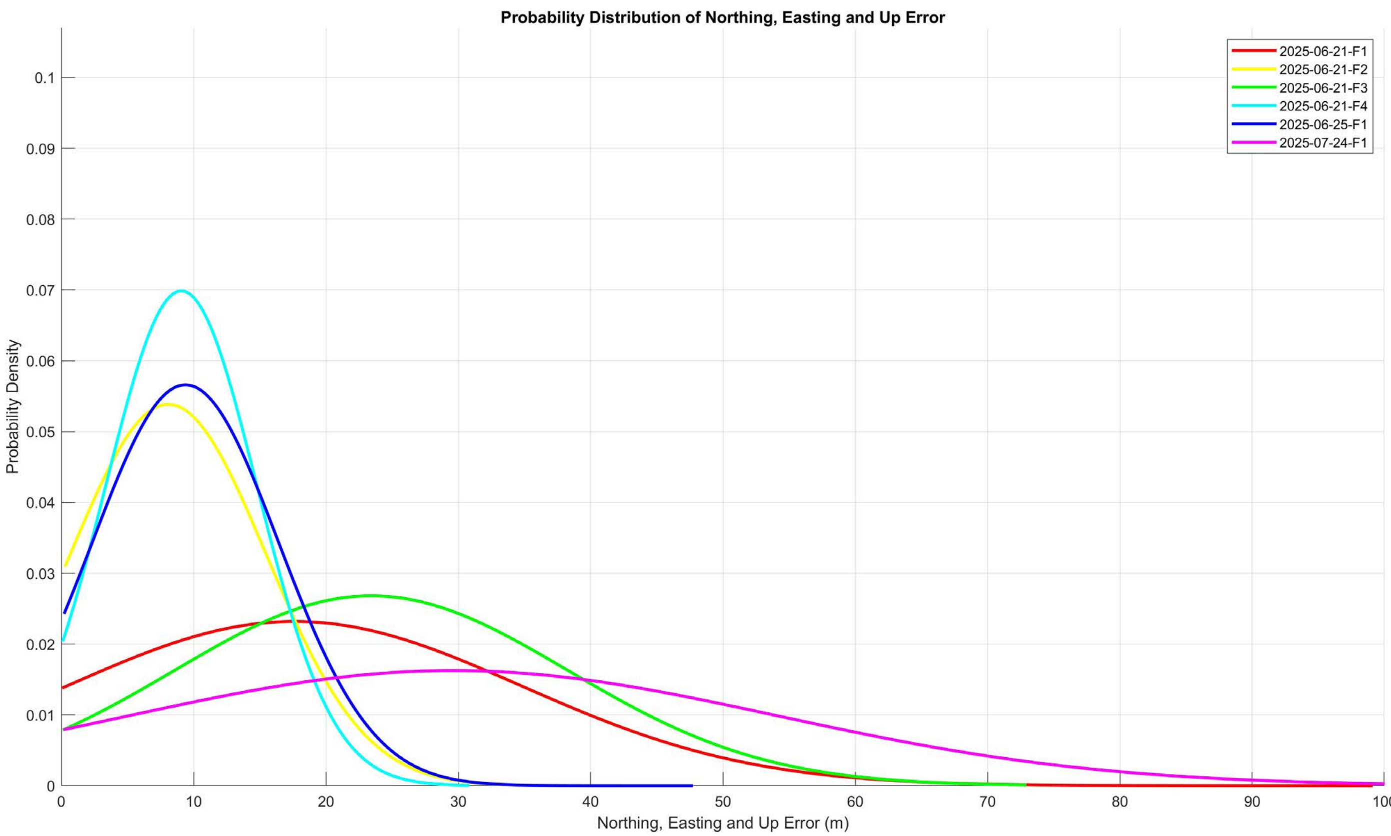

Figure 7.4. 3D Position Error Probability plot

Figure. 7.5 shows the global probability distribution of the combined Northing, Easting, and Up positional errors. The calculated mean error is 18.08 meters, showing the capability of the system to perform with low drift while flying at low altitudes over difficult terrain. The distribution is positively skewed, meaning that smaller errors occur more frequently, and that errors beyond 80 meters are improbable.

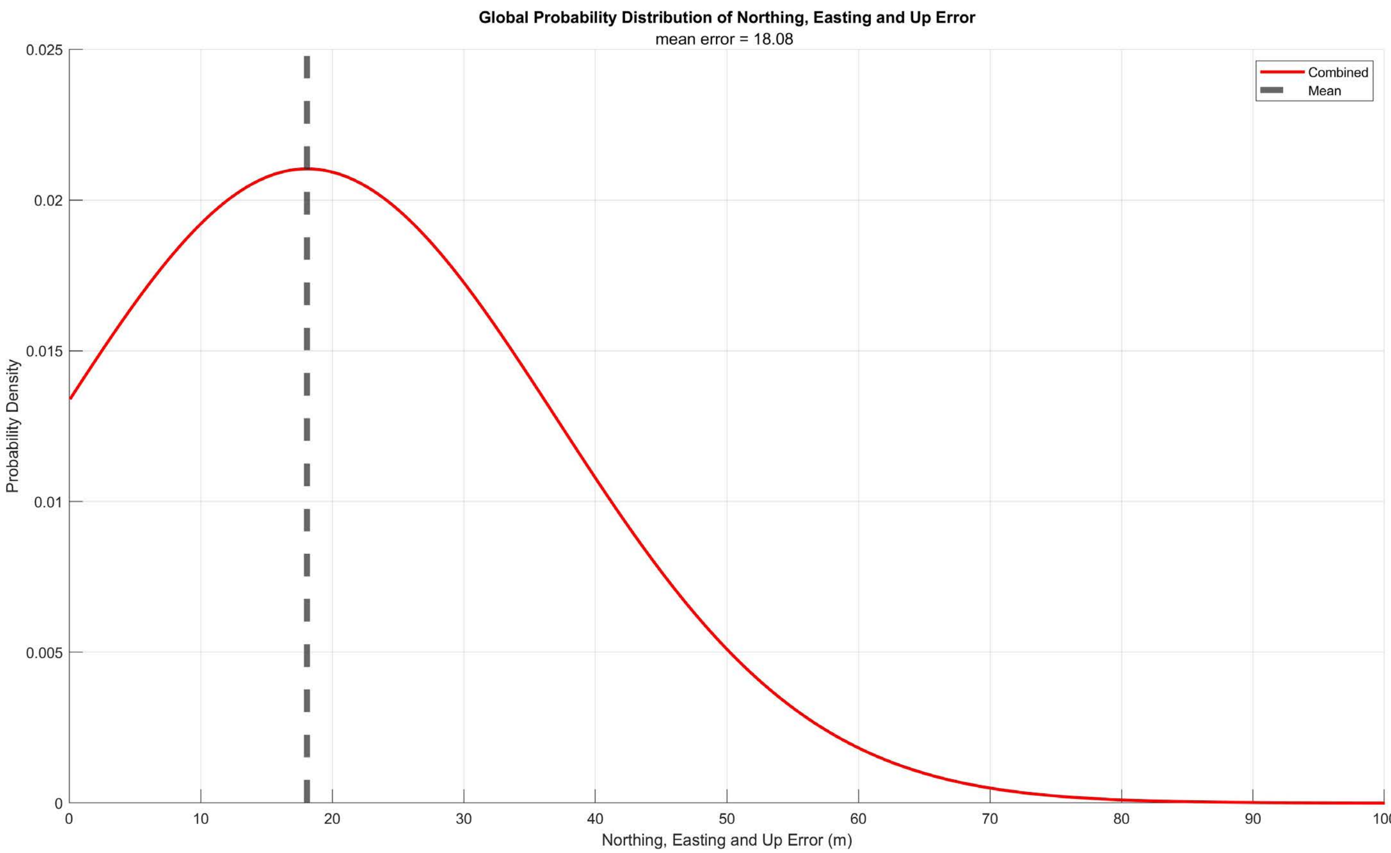

Figure 7.5. Global Probability for Northing, Easting, and Up Error

Figure. 7.6 presents the error growth rate per unit distance traveled, expressed as percentage per kilometer. Across all flights error rate is typically highest during the initial stages, typically falling below 0.1%/km after 20 km. Dataset 2025-07-24-F1 experienced a greater peak during the flight, jumping to roughly 0.2%/km, however it was able to recover to an error rate of below 0.05%/km afterward. Overall, the plot indicates that even if the system experienced short periods of increased drift, particularly in the early and mid-flight phases, it maintained long stretches of low error accumulation, demonstrating strong positional stability over extended distances in GNSS-denied conditions.

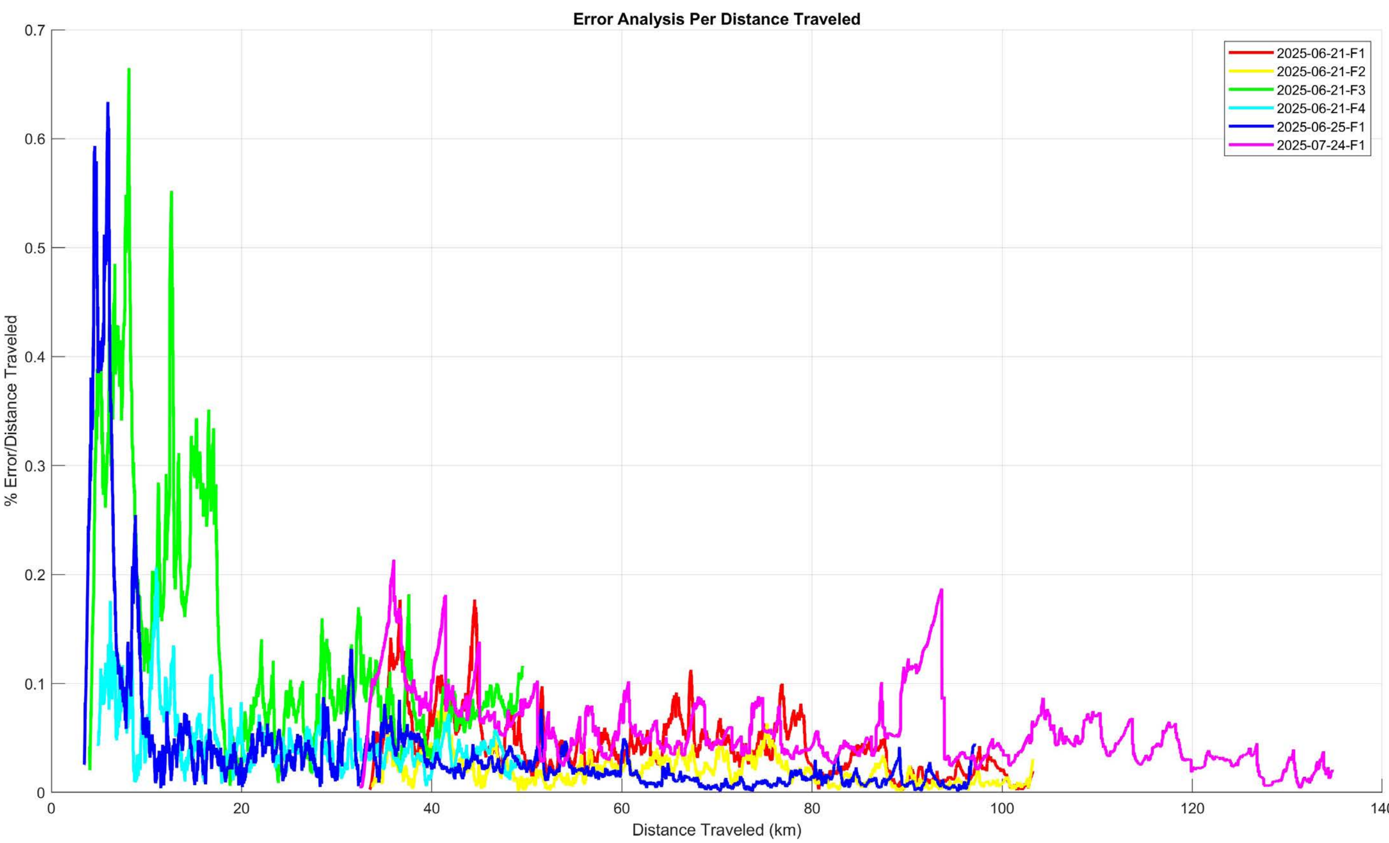

Figure 7.6. Error Analysis per Distance Traveled

Figure. 7.7 presents the probability distribution of the normalized position error growth rate, expressed as percentage per unit distance traveled. The majority of datasets were concentrated at lower %/distance values, indicating the capacity of VINS with VPS and VIO to maintain high positional stability.

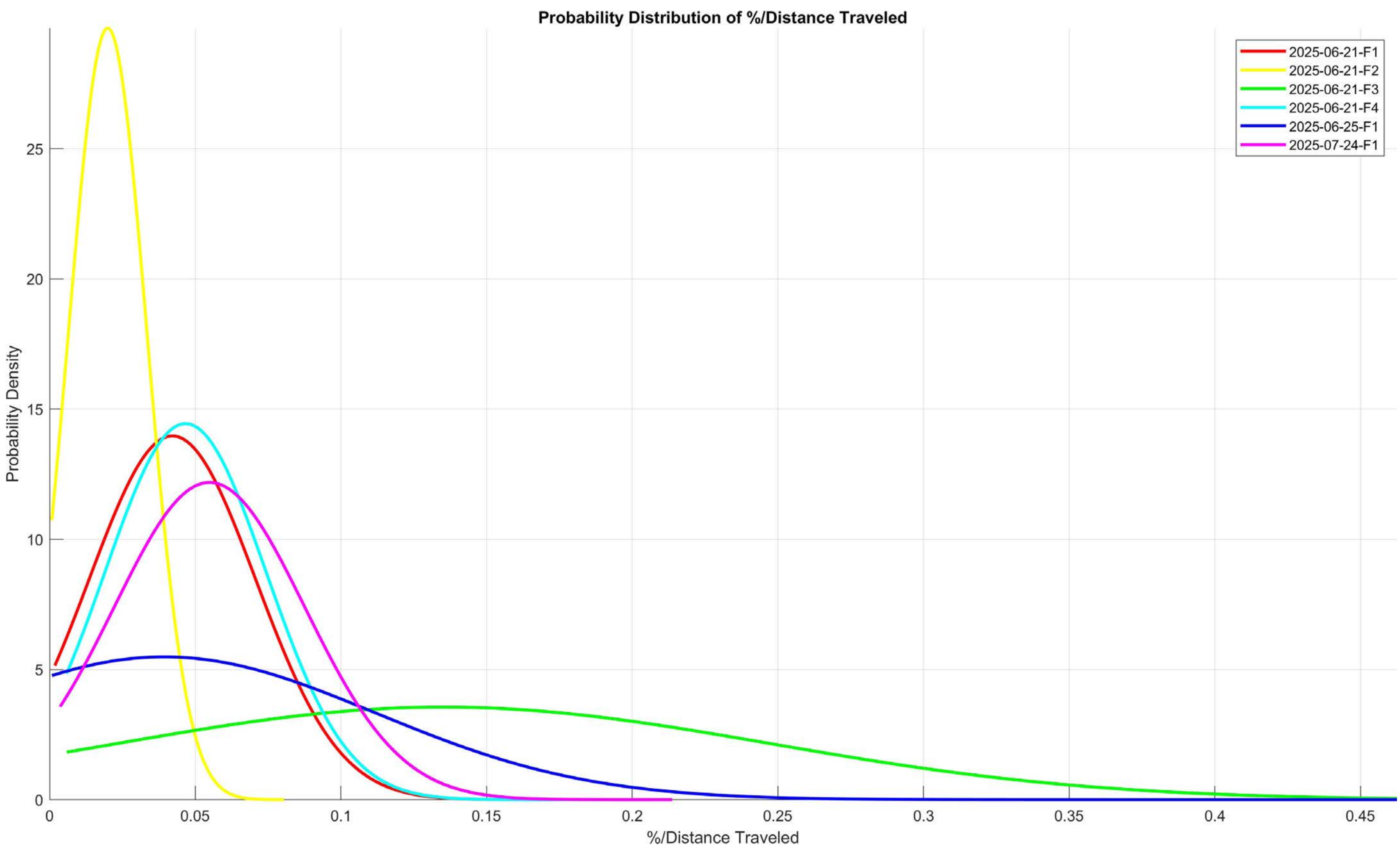

Figure 7.7. Easting, Northing and MSL error vs DT in percentage

8. Conclusion

Based on the results of the 18 flight tests, several key conclusions can be drawn regarding the performance of the integrated VINS with VIO and VPS. Overall, the system achieved a mean error of 16.55 meters, with the infrared camera solution demonstrating slightly better performance (15.88 meters) compared to the daylight camera (18.08 meters). While this does indicate an advantage for the infrared configuration, the difference is not substantial enough to discourage the use of the daylight camera, which remains a viable option. Furthermore, the system achieved a CEP50 of 13.22 meters over a 50 km trajectory, underscoring its ability to deliver consistent accuracy. Overall the system maintained reliable tracking performance across a wide range of altitudes and under diverse GNSS-denied conditions, demonstrating the robustness and operational suitability of the solution for contested and constrained environments.

Table 8.1. Flights performance

Flight Date and Number	Position Error (m)	Maximum AGL (m)	Average AGL (m)	Flight Duration (min)	Flight Time in GNSS-Denied (min)	Distance Traveled (GNSS-Denied) (km)
2025-04-28-F1	14.32	1070.37	602.59	30.88	23.25	69.73
2025-04-28-F2	8.70	856.33	586.25	28.59	20.22	48.50
2025-04-28-F3	12.17	981.43	558.54	23.71	19.06	56.77
2025-06-05-F1	18.31	2078.25	1024.42	49.81	44.13	125.56
2025-06-05-F2	7.15	346.17	256.36	22.07	15.36	40.26
2025-06-21-F1	17.60	362.28	227.88	40.23	22.09	69.77
2025-06-21-F2	8.08	363.63	229.88	40.03	21.88	69.53
2025-06-21- F3	23.42	350.45	188.95	22.07	15.49	45.56
2025-06-21-F4	9.07	350.26	190.10	21.99	15.10	44.70
2025-06-25-F1	9.38	339.39	251.18	34.33	31.19	93.68
2025-07-10-F1	7.81	667.33	316.07	32.09	24.84	77.77
2025-07-10-F2	9.92	570.50	329.27	22.74	18.90	52.84
2025-07-10-F3	14.78	999.12	555.89	22.79	21.84	62.15
2025-07-10-F4	35.09	999.79	558.91	22.68	21.79	62.36
2025-07-22-F1	14.72	1285.08	922.00	36.81	28.32	101.15
2025-07-22-F2	11.38	1286.80	924.53	36.81	28.35	101.31
2025-07-22-F3	25.28	789.48	395.72	47.41	46.28	152.61
2025-07-24-F1	29.60	712.23	377.74	38.61	28.88	102.23

8. Revision History

Table 11.1. Change Status Log

Revision	Date	Affected paragraphs	Remarks
1.0	Aug 22, 2025	All	Initial release.

Contact Us: +1 (703) 880-4222 | (+1 844 468 4284).

Address: 39959 Catoctin Ridge Street, Paeonian Springs, VA 20129 U.S.A.

multipletestanalysis-tr-il-nse-ae
30194631 900 1025